

MINFLUX nanoscopy delivers 3D multicolor nanometer resolution in cells

Klaus C. Gwosch 1,4, Jasmin K. Pape 1,4, Francisco Balzarotti 1,4, Philipp Hoess 2, Jan Ellenberg 2, Jonas Ries 2 and Stefan W. Hell 1,3*

The ultimate goal of biological super-resolution fluorescence microscopy is to provide three-dimensional resolution at the size scale of a fluorescent marker. Here we show that by localizing individual switchable fluorophores with a probing donut-shaped excitation beam, MINFLUX nanoscopy can provide resolutions in the range of 1 to 3 nm for structures in fixed and living cells. This progress has been facilitated by approaching each fluorophore iteratively with the probing-donut minimum, making the resolution essentially uniform and isotropic over scalable fields of view. MINFLUX imaging of nuclear pore complexes of a mammalian cell shows that this true nanometer-scale resolution is obtained in three dimensions and in two color channels. Relying on fewer detected photons than standard camera-based localization, MINFLUX nanoscopy is poised to open a new chapter in the imaging of protein complexes and distributions in fixed and living cells.

hile STED1,2 and PALM/STORM3,4 fluorescence microscopy (nanoscopy) can theoretically achieve a resolution at the size of a single fluorophore, in practice they are typically limited to about 20 nm. Owing to a synergistic combination of the specific strengths of these key super-resolution concepts, the recently introduced MINFLUX nanoscopy⁵ can attain a resolution of about the size of a molecule, in principle without constraints from any wavelength, numerical aperture or molecular orientation (Supplementary Note). In MINFLUX imaging, the fluorophores are switched individually like in PALM/STORM, whereas the localization is accomplished by using a movable excitation beam featuring an intensity minimum, such as a donut. Ideally, the minimum is a zero-intensity point that is targetable like a probe⁶. Concomitantly, it serves as a reference coordinate for the unknown position of the fluorophore in the sample, because the closer the minimum is to the fluorophore, the weaker the emitted fluorescence per unit excitation power. So if the excitation zero and the fluorophore coincide in space, fluorescence will cease. However, the position of the emitter will be known in that case, as it will be the perfectly controlled position of the excitation intensity zero. For the same reason, the smaller the mismatch between the two coordinates is, the fewer emitted photons are required to measure the position of the emitter. Hence, approaching a fluorophore with a position-probing excitation minimum shifts the burden of requiring many photons for localization from the feeble fluorescence of an individual emitter to the inherently bright excitation beam. Thus, MINFLUX gains a fundamental edge over localization by calculating the centroid of a faint fluorescence diffraction pattern produced by the fluorophore on a camera.

While the resolution and speed advantage of MINFLUX nanoscopy have been documented^{5,7}, here we demonstrate that it also allows for three-dimensional (3D) imaging and simultaneous two-color registration, which are critically important for life science applications. Moreover, we show that, in conjunction with photoactivatable fluorescent proteins, MINFLUX affords true nanometer-scale resolution in living cells. The first realization of MINFLUX utilized static distances of the intensity zero to the fluorophore,

which limited the imaged field to extents of $100 \times 100 \,\mathrm{nm^2}$ or less⁵. Here we dynamically zoom-in on each fluorophore position, which not only renders the localizations essentially uniform and isotropic, but also facilitates the recording of extended areas and volumes.

Results

Basics on iterative fluorophore targeting with a local excitation minimum. The power of zooming-in on each fluorophore is illustrated for a fluorophore located at $x_{\rm M}$, within the interval $x_{\rm 0} < x_{\rm M} < x_{\rm 1}$ of size $L = |x_1 - x_0|$. When probing with an intensity zero that is flanked by a quadratic intensity profile, it is sufficient to measure the number of fluorescence photons $n(x_0)$ and $n(x_1)$ with the zero placed at the interval endpoints⁵. With $n(x_0)$ and $n(x_1)$ following Poissonian statistics, the minimum s.d. of the localization, that is the Cramér–Rao bound (CRB) within the region L, is given by $\sigma \ge \frac{L}{4\sqrt{N}}$ with $N = n(x_0) + n(x_1)$. Contrasting the linear dependence on the interval size L with the inverse square-root dependence on the number of detected photons N shows that reducing L, that is, zooming-in on the molecule, outperforms the wait for more photons.

This also becomes evident when approaching $x_{\rm M}$ in successive steps with stepwise reduced L_k , such that L_k is chosen to match three times σ_{k-1} , that is, the uncertainty of the previous step. Thus, after k iterations we obtain a total of $N_{\rm t}=k\cdot N$ detected photons and a CRB of

$$\sigma_k \ge \frac{L_k}{4\sqrt{N}} = \frac{3 \cdot \sigma_{k-1}}{4\sqrt{N}} = \frac{3 \cdot L_{k-1}}{\left(4\sqrt{N}\right)^2} = \dots = \frac{3^{k-1}}{\left(4\sqrt{N}\right)^k} L_1 \propto k^{k/2} \frac{L_1}{N_t^{k/2}}$$

underscoring once more that it is more effective to increase the number of iterations k than the photons per iteration N. Already four steps (k=4) yield $\sigma_4 \propto 1/N_{\rm t}^2$, which is an inverse quadratic as opposed to an inverse square-root dependence on the total number of detected photons. More iterations yield an even higher order, accounting for the fact that the detected photons become more informative the closer the probing positions are to the molecule.

¹Department of NanoBiophotonics, Max Planck Institute for Biophysical Chemistry, Göttingen, Germany. ²Cell Biology and Biophysics Unit, European Molecular Biology Laboratory (EMBL), Heidelberg, Germany. ³Department of Optical Nanoscopy, Max Planck Institute for Medical Research, Heidelberg, Germany. ⁴These authors contributed equally: Klaus C. Gwosch, Jasmin K. Pape, Francisco Balzarotti. *e-mail: stefan.hell@mpibpc.mpg.de

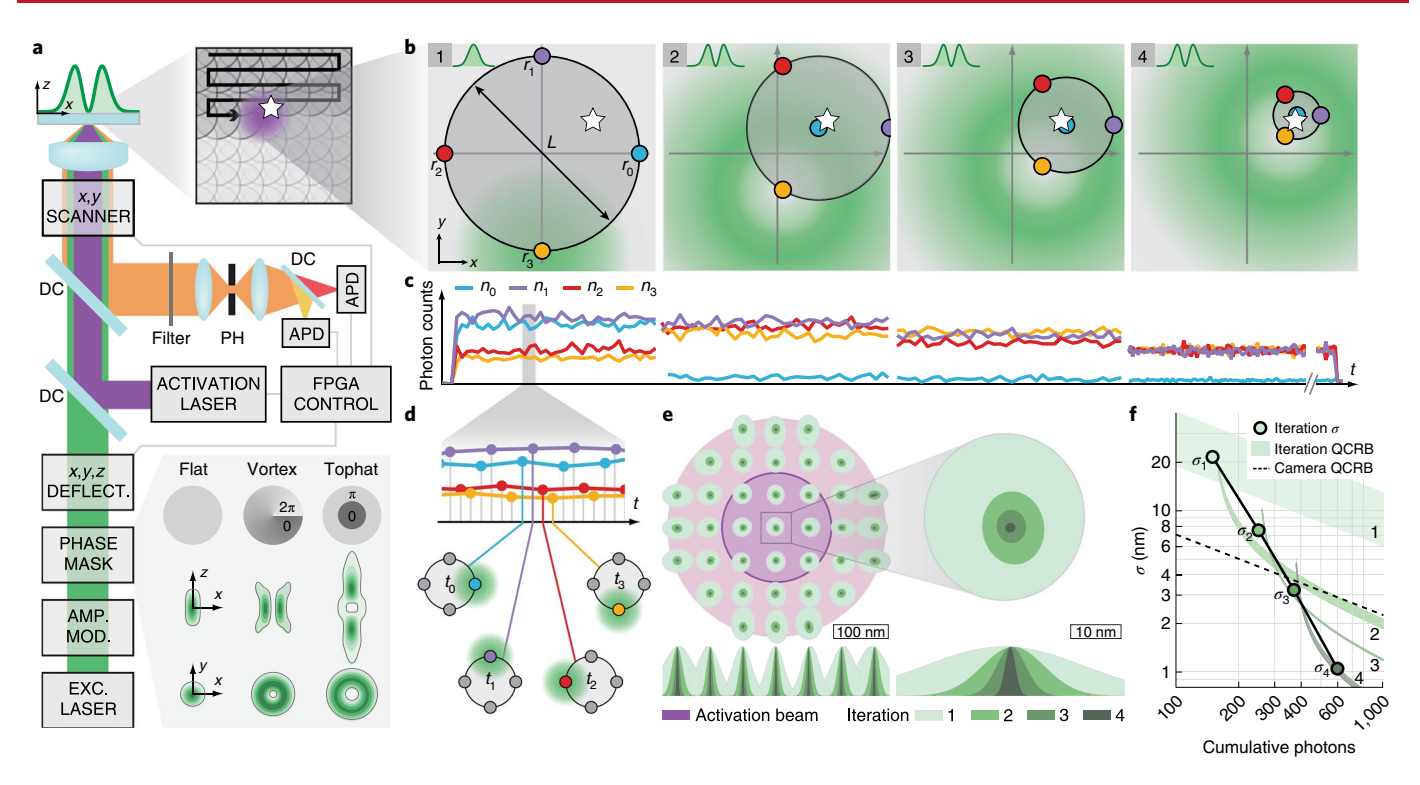


Fig. 1 | Iterative MINFLUX setup and localization. a, Setup. An excitation beam (green) is amplitude- and phase-modulated (bottom right inset; flat (regular focus), vortex (2D donut), tophat (3D donut)), electro-optically deflected in x,y,z, overlapped with a photoactivation beam (purple) and focused into the sample after passing a piezo-actuated mirror for coarse xy scanning (top right inset; white star, activated molecule position). Fluorescence is descanned, deflected by a dichroic mirror (DC), filtered by a confocal pinhole (PH), split in two spectral ranges by another dichroic mirror and detected by photon-counting avalanche photodiodes (APDs) (all controlled by FPGA boards). **b**, Iterative xy localization by targeting the beam to four designated coordinates constituting the TCP (blue, purple, red, yellow and beam on yellow position in green). Step 1, regular focus; steps 2-4, 2D donut. The TCP is recentered and zoomed-in on the fluorophore (white star) in steps 2-4. **c**, Typical fluorescence counts for each iteration with the color indicating the targeted coordinate. **d**, Representation of the interleaved TCP measurement. **e**, Convergence of iterative localizations for molecules within the activation area (purple, 200 nm FWHM, 50% single molecule activation probability; pink, 2-FWHM, 95% activation probability). The covariance of each iteration (green shades) is represented as an ellipse of $e^{-1/2}$ level. **f**, Progression of the spatially averaged localization precision $\sigma_1 - \sigma_4$ for each iteration (green dots) with the corresponding CRBs (green shades) and the CRB for standard camera-based localization (dashed line). **e,f**, Photons, $N_1 = 150$, $N_2 = 100$, $N_3 = 120$ and $N_4 = 230$, total $N_t = 600$; TCPs, $L_{1,reg} = 300$ nm, $L_{2,donut} = 150$ nm, $L_{3,donut} = 90$ nm and $L_{4,donut} = 40$ nm.

In practice, this procedure is only limited by the background photons, which compromise the information on where to place the zero next.

Realizing iterative MINFLUX and scalable fields of view. Our setup is a beam-scanning confocal fluorescence microscope featuring an excitation beam that can enter the objective lens with a flat wavefront, hence being regularly focused, as well as amplitude- and phase-modulated to form a donut in the focal region (Fig. 1a and Supplementary Fig. 1; Methods). The excitation beam is co-aligned with a UV beam for activating individual emitters in a ~400 nm diameter region in the sample (Fig. 1a,e). Micrometer-range positioning or scanning of these co-aligned beams is performed with a piezo-based mirror, whereas microsecond nanometer-range targeting is carried out using an electro-optic beam deflector.

Like all fluorescence nanoscopy concepts, MINFLUX nanoscopy relies on a fluorescence on–off transition for the separation of neighboring emitters. We transiently activated a single fluorophore within the activation region (~400 nm diameter), localized it by MINFLUX and finally let it return to a lasting off-state. The same procedure was applied to the next fluorophore until a representative number of molecules was registered. For each localization, we targeted the zero to a set of coordinates around the anticipated fluorophore position, referred to as the targeted coordinate pattern (TCP). Forming a circle in the focal plane, the diameter *L* of the TCP is a measure of how well the TCP is zoomed-in on the molecule (Fig. 1b).

In the first iteration, the beam was focused regularly, while in the succeeding steps it was phase modulated to form a 2D or 3D donut, depending on whether we localized the fluorophore just in the focal plane (x,y) or in the sample volume (x,y,z), respectively. In each iteration, we calculated the newly anticipated fluorophore position on the basis of collecting a defined number of photons in the fluorescence traces (Fig. 1c) produced at each of the targeted coordinates (Fig. 1d). The four-point TCP used for 2D localization rendered the position estimator simple and unambiguous⁵. In the next iteration, the TCP was centered on the new position and the diameter L decreased according to the new precision estimate, thus bringing the zeros closer to the molecule. To compensate for the associated reduction in excitation intensity and to maintain the fluorescence flux, we increased the excitation power in each step. The smallest L in the last iteration step, which conveyed how well we could zoom-in on the fluorophore, was determined by the concomitantly decreasing signal-to-background ratio.

We first simulated the procedure by randomly generating multinomial photon counts for different molecule positions, applying four iteration steps and zero background (Methods). On average, our iteration procedure (Fig. 1b) achieved a localization precision of $\sigma_{1D} \approx 1$ nm with only $N_t = 600$ photons (Fig. 1f). In contrast to static (non-iterative) MINFLUX localization⁵, the precision obtained here was largely isotropic and independent of the emitter position within the activation area (Fig. 1e). In our simulation, we selected different

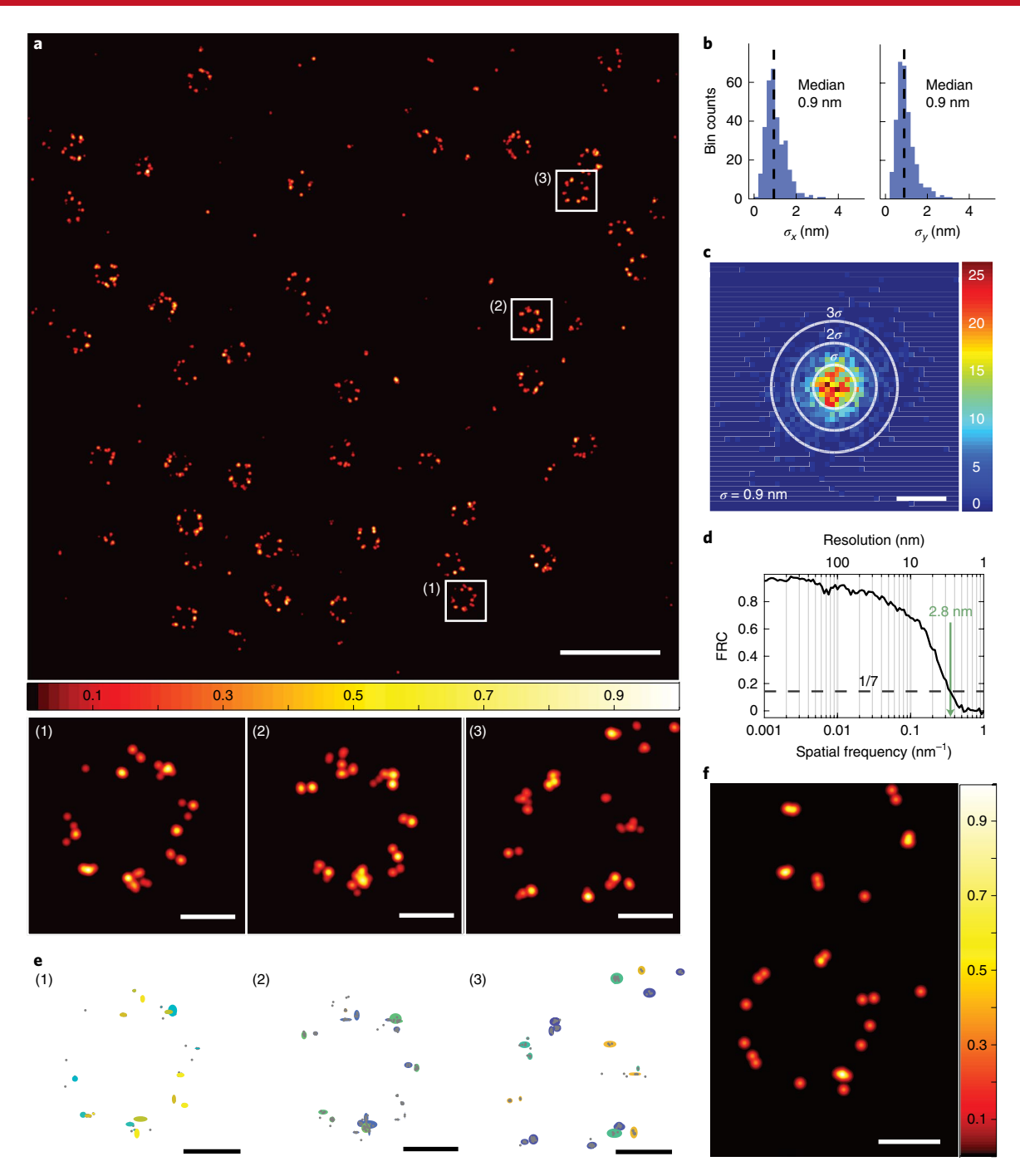


Fig. 2 | MINFLUX nanoscopy in fixed and living cells. **a**, MINFLUX nanoscopy of a U-2 OS cell expressing Nup96-SNAP labeled with Alexa Fluor 647. Single-molecule fluorescence events were split into bunches of 2,000 photons, yielding localizations that are filtered and displayed as described below (Methods; Supplementary Fig. 4). Zoomed-in excerpts (below) show single nuclear pores, with each dot highlighting groups of localizations representing individual proteins through their fluorescent labels. **b**, Histograms of s.d. of localizations from single molecules in *x* and *y*. Only molecules providing >4 localizations per trace were considered. **c**, Histogram of the distance of a localization to the mean position of a single emitter. The ellipses are displayed with major axes of 2σ , 4σ and 6σ in length, respectively, with σ being determined in a 1D Gaussian fit. **d**, FRC curve for the image in **a**. **e**, Renditions of insets of **a** with 3σ ellipses for each molecule. Colors indicate assignment of localizations to a single molecule on the basis of splitting of emission events. **f**, MINFLUX image of nuclear pores in living U-2 OS cell expressing Nup96-mMaple; ~40 localizations with an average of ~1,600 detected photons per localization. Scale bars, 500 nm (**a**), 50 nm (**a** (insets),**e**,**f**) and 2 nm (**c**).

photon numbers in each step according to the required precision, with the last step featuring the largest photon number. The precision still largely followed the anticipated $1/N_{\rm t}^2$ behavior. Starting with a lower photon efficiency, our iterative MINFLUX scheme

surpassed the quantum CRB (QCRB)⁸ of lateral precision for standard camera-based localization with $N_{\rm t} \approx 330$ photons (Fig. 1f).

For imaging, we defined a state machine on a field-programmable gate array (FPGA) board that recognized single activated

fluorophores and localized them iteratively (Methods; Supplementary Fig. 2 and Supplementary Table 1). We actively stabilized the sample during measurements to avoid drift (Methods; Supplementary Fig. 3). Individual emitters were identified by segmenting their emission trace and their position was obtained by maximum-likelihood estimation (Methods). Events with low photon counts or incorrect TCP centering were discarded (Methods; Supplementary Fig. 4). First, we imaged Nup96, a protein of the nuclear pore complex (NPC), labeled with the organic fluorophore Alexa Fluor 647 using SNAP-tag in fixed mammalian (U-2 OS) cells⁹ (Fig. 2a; Methods). Images of several micrometers in size, limited to roughly 10×10 µm² by the available scan range, were acquired using MINFLUX with five iteration steps ($N_1 = 100$, $N_2 = 100$, $N_3 = 150$, $N_4 = 300$ and $N_5 \approx 2,000$, and $L_{1,reg} = 300 \,\text{nm}$, $L_{2,reg} = 300 \,\text{nm}$, $L_{3,\text{donut}} = 150 \,\text{nm}$, $L_{4,\text{donut}} = 100 \,\text{nm}$ and $L_{5,\text{donut}} = 50 \,\text{nm}$). On the basis of these parameters and the background (Supplementary Fig. 5), we expected a localization precision below 1 nm in s.d. The overall fluorescence rate of typically ~50 kHz allowed a complete localization within ~40 ms. To ensure a single active fluorophore per activation area, 0.5-5 µW of UV light was applied in pulses of 0.5 ms until a fluorescent molecule appeared. To avoid simultaneous activation of several fluorophores, we interrupted the activation laser upon appearance of a single fluorophore emission (Methods). After activation and registration of a single Alexa Fluor 647 molecule, the iterative scheme took around 10 ms to reach the final iteration. The photon traces and the TCP readjustment were monitored during recording. Altogether, the acquisition of a single NPC required about 1-2 min resulting in about 100 localizations. The recording time of the entire field of view was about 60 min. Our experiments demonstrated that iterative MINFLUX clearly resolved the eightfold symmetry of Nup96 in single NPCs (Fig. 2a), distributed along a ring of 107 nm in diameter^{9,10}. In fact, the localizations typically formed eight clusters of roughly two to four localization subclusters, displayed as the sum of Gaussian distributions, one for each localization (Methods), revealing what was most likely individual Nup96 proteins through their individual fluorescent markers (Supplementary Fig. 6). This molecular-scale resolution is obtained in various images of the nuclear envelope, demonstrating that iterative MINFLUX nanoscopy can accommodate fields of any size and shape, just like any scanning confocal microscope.

To provide quantitative resolution measures, we applied three different criteria (Fig. 2b-d; Methods). First, we calculated the s.d. σ for five or more localizations per fluorophore, where each localization utilized ~2,000 photons of the last iteration, extracted from over 300 single fluorophore events. The resulting distribution of σ featured a median of ~1 nm (Fig. 2b). Another resolution assessment was gained by subtracting the mean localized position of an emission train from all of its single localizations (Fig. 2c). Assuming a Gaussian distribution, we obtained a precision error $\sigma_{1D} = 0.9$ nm. In the third approach, we calculated the Fourier ring correlation (FRC) curve^{11,12} of the localization data (Fig. 2d), which better captured the influence of setup instabilities on the effective resolution. The threshold value of 1/7 gave $\Delta_{FRC} \approx 3$ nm as a resolution estimate. Simulating localizations at the expected Nup96 positions with a fixed localization s.d. revealed that this experimental FRC resolution Δ_{FRC} corresponded to a localization precision of roughly 1 nm. To represent the obtained precision in an actual image, we displayed individual localizations with covariance ellipses of 3σ for each emission (Fig. 2e).

As Alexa Fluor 647 imposes a number of restrictions on the sample preparation, most notably incompatibility with living cells, we next demonstrated that MINFLUX nanoscopy is viable with photoactivatable fluorescent proteins. We resolved the eightfold symmetry of Nup96 tagged with the photoconvertible protein mMaple (Methods; Supplementary Table 2) in both fixed and living cells (Fig. 2f and Supplementary Fig. 7a) with a localization precision of ~2 nm (Supplementary Fig. 7b). In particular, the live-cell recording

proves that imaging of protein complexes in the interior of living cells is possible with nanometer resolution.

3D MINFLUX imaging with isotropic resolution. Dissection of macromolecular complexes calls for 3D resolution and hence for usage of the 3D donut (Fig. 3a). In our 3D localization algorithm, we probe the molecule position with three different TCPs. First, the xy position is probed with a regularly focused beam, so that the central z axis of the 3D donut is positioned as closely as possible to the fluorophore. Next, the 3D donut is targeted in two positions above and below the anticipated fluorophore position. Last, three coordinate pairs on the x, y and z axes and also the center coordinate of this arrangement are addressed, resulting in a 3D position estimate. A simulation of this 3D MINFLUX algorithm (Fig. 3b) showed that 1,000 detected photons were sufficient to cover a ~400 nm diameter volume with a largely homogenous and isotropic 3D precision of ~1 nm (Fig. 3c-d). Again, the increase in precision with the total number of detected photons proved to be steeper than $1/\sqrt{N_t}$ (Fig. 3e). Comparing the result with the QCRB for the precision of camera-based localization shows that 3D MINFLUX can outperform all standard camera-based approaches, including multiple-objective lens arrangements.

The axial position of the 3D donut was controlled with an electrically tunable lens, allowing refocusing within a range of ~400 nm within 50 µs. Imaging Nup96-SNAP-Alexa Fluor 647 (Fig. 3f, Supplementary Fig. 3 and Supplementary Video 1; Methods), 3D MINFLUX discerned the cyto- and nucleoplasmic layers of Nup96 in single pore complexes (Fig. 3g). As the cell lay flat on a cover slip, these layers were typically parallel to the focal plane and ~50 nm apart in the z direction⁹. 3D MINFLUX also recovered the curvature of the nuclear envelope extending ~300 nm in depth within the acquired region (Fig. 3f). The localizations featured one-dimensional (1D) s.d. of $\sigma_{xy} = 2.4 \,\text{nm}$ and $\sigma_z = 1.7 \,\text{nm}$ (Fig. 3h). Localizations from single events exhibited median s.d. of $\sigma_{xy} = 2.6 \,\text{nm}$ and $\sigma_z = 1.8 \,\text{nm}$, respectively (Fig. 3i). Note that the refractive index mismatch at the glass-water interface caused a slight difference between the xy and z localization precision, as L_z of the TCP was slightly compressed owing to this mismatch¹³, increasing the MINFLUX localization precision accordingly (Methods).

Next, we imaged the protein PSD-95 in dissected hippocampal neuron cultures from transgenic mice expressing a fusion protein of the Halo-Tag enzyme connected to the protein C terminus¹⁴ (Fig. 4a,b, Supplementary Fig. 3 and Supplementary Video 2; Methods). PSD-95 putatively plays a key role in anchoring and rearranging glutamate receptors in the post-synaptic membrane 15,16. 3D MINFLUX nanoscopy suggested that PSD-95 is arranged along a slightly curved surface of 100-400 nm side length. The spots of a high localization density exhibited a s.d. of ~4-6 nm, with the localization precision being estimated to $\sigma_{1D} \approx 2-3$ nm (Fig. 4c). The average distance between nearest-neighbor clusters was ~40 nm. While super-resolution techniques were repeatedly used to elucidate the organization of post-synaptic proteins¹⁷, virtually all superresolution studies were carried out in 2D. Owing to its isotropic resolution, 3D MINFLUX now opens up entirely new possibilities for studying synaptic protein organization.

Multicolor MINFLUX imaging. Fluorophore species sharing the same excitation wavelength but having measurable differences in their emission spectra, such as Alexa Fluor 647, CF660C and CF680 (ref. ¹⁸) can be separated by spectral classification. Hence, we split the fluorescence at 685 nm into two spectral fractions using a dichroic mirror, and detected both fractions with photon-counting detectors. While localization was performed by adding up the photons from both detectors, comparing the counts of each spectral fraction enabled fluorophore classification (Methods). The classification was refined using principal component analysis on the spectral fractions from all MINFLUX iterations and selecting a classification threshold on the basis of the

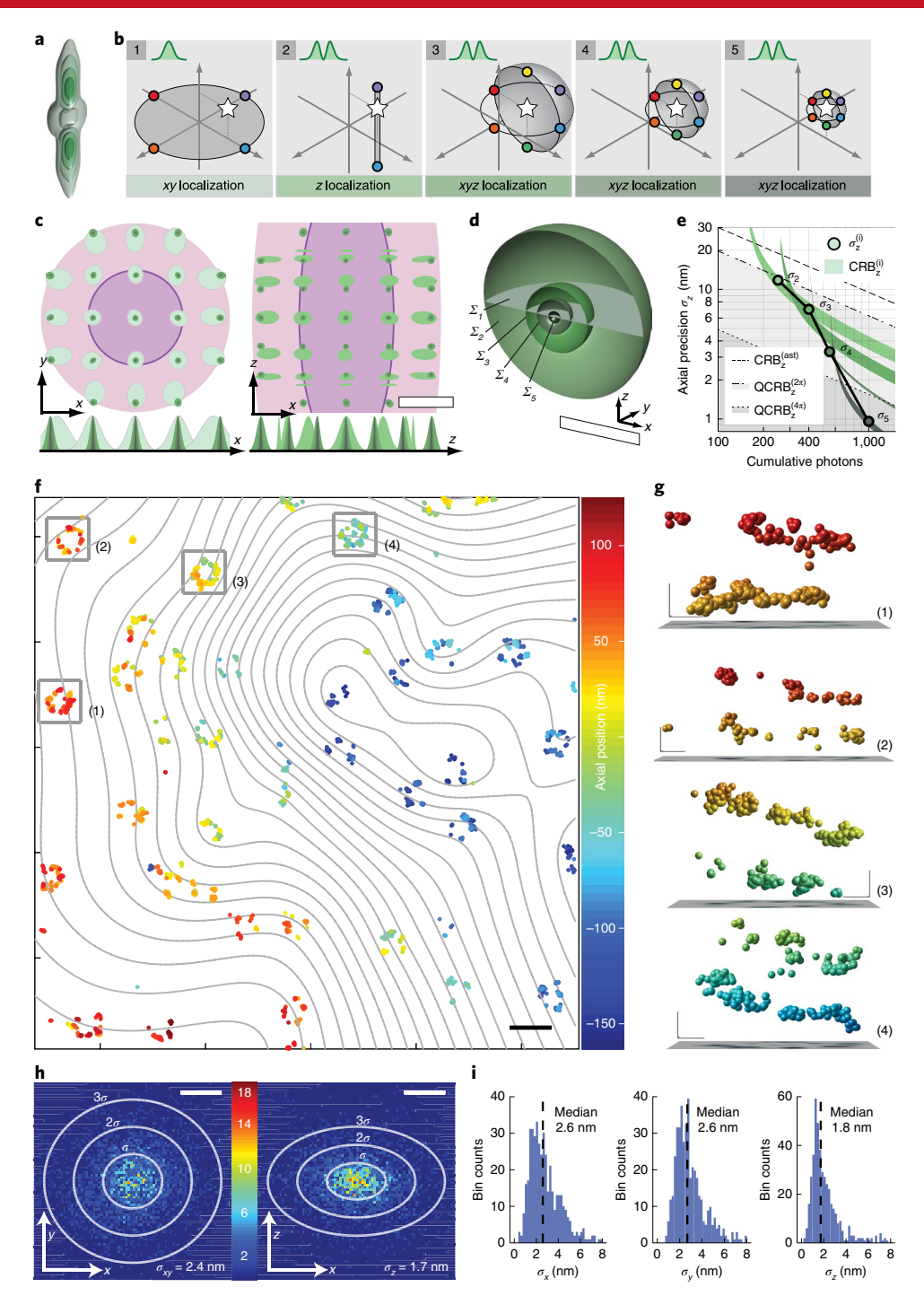


Fig. 3 | Iterative 3D MINFLUX localization yields isotropic nanometer precision. **a**, 3D donut with selected isointensity surfaces. **b**, Iterations. Step 1, xy localization with a regularly focused beam (top left, intensity profile). Step 2, z localization with the 3D donut. Steps 3–5, x, y, and z localization with the 3D donut, shrinking the TCP each time. **c**, Simulation of localization convergence in xy (left) and xz (right) for molecules within the activation region (purple, 200 nm FWHM_{xy} and 600 nm FWHM_z with 29% activation probability; pink, 2·FWHM with 86% activation probability). The covariance of each iteration (green shades) is represented as an ellipse at level e^{-1/2}. **d**, 3D representation of the step-wise localization precision in the central region in **c**. **e**, Progression of average z precision in **c** (dots), showing the CRB for standard camera-based astigmatic localization, the QCRB for a camera localization in a 2π and 4π arrangement (dashed lines) along with MINFLUX CRB in each iteration (green shades). **c-e**, Photons, N_1 =150, N_2 =100, N_3 =150, N_4 =150 and N_5 =450; total N_t =1000. Step 1, regular focus with $L_{1,reg}$ =300 nm. Steps 3–5, 3D donut with $L_{2,3D-donut}$ =400 nm, $L_{3,3D-donut}$ =150 nm, $L_{4,3D-donut}$ =90 nm and $L_{5,3D-donut}$ =40 nm. **f**, MINFLUX image of nuclear pore complexes of a fixed cell (Nup96-SNAP-Alexa Fluor 647); the z coordinate is color-coded. Contour lines indicate the nuclear envelope. **g**, z sections of single nuclear pores in **f**. **h**, Localization precision for 3D imaging in xy (left) and xz (right). **i**, Histograms of x, y and z s.d. Scale bars, 100 nm (**c**), 10 nm (**d**), 200 nm (**f**), 20 nm (**g**), 5 nm (**h**).

distribution of the first principal component. We first tested two-color 2D MINFLUX imaging on a DNA origami labeled with Alexa Fluor 647 and CF660C molecules, arranged at distances of $\sim\!10\,\text{nm}^{19}$

(Fig. 5a and Supplementary Fig. 4). MINFLUX nanoscopy delivered one-dimensional localization distributions of 1.3–2 nm full width at half maximum (FWHM) corresponding to $\sigma \lesssim 1$ nm (Fig. 5b,e). The

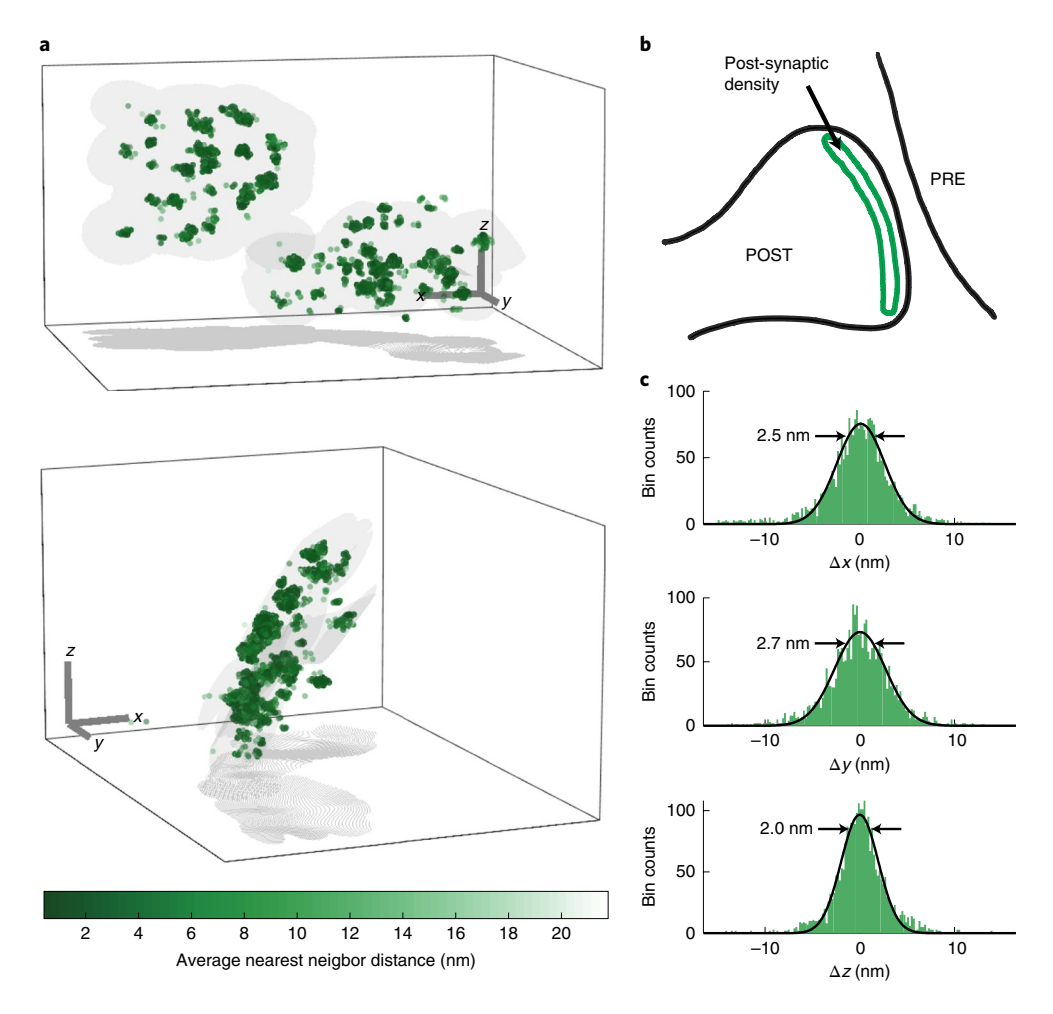


Fig. 4 | MINFLUX imaging of the post-synaptic protein PSD-95 with 3D resolution of 2-3 nm s.d. Hippocampal neurons from transgenic mice expressing PSD-95-Halo conjugated to Alexa Fluor 647 after fixation were used as sample. **a**, Two projections (top, bottom) of a 3D MINFLUX image with color indicating the 3D density of molecular localizations. PSD-95 appears in clusters distributed on a curved surface (gray surface) displayed also as a contour line projection to the *xy*-bounding plane. Scale bar, 100 nm. **b**, Sketch of PSD-95 occurrence at the postsynaptic site. **c**, Histograms of distances of localizations to the mean molecule position in *x*, *y* and *z*, revealing an isotropic 3D localization precision of the individual fluorophores of 2.0-2.7 nm s.d.

two fluorophore species were distinguished without overlap (Fig. 5d). Moreover, chromatic distortions between the two color channels are excluded on principle grounds, as the localization is performed by the same excitation beam. This is in contrast to camera-based localization, where nanometer multicolor co-localization usually suffers from chromatic aberrations of the optical system.

Finally, we acquired two-color 3D images of the nuclear pores in U-2 OS cells by labeling the NPC with wheat germ agglutinin (WGA) conjugated to CF680 in addition to the Nup96–SNAP–Alexa Fluor 647 decoration²⁰. We observed the CF680 residing inside the Nup96 octamer both laterally and axially (Fig. 5c,g and Supplementary Video 3). Although the emitters featured a broader spectral distribution in the cell than in the origami, we could classify the labels with high fidelity (Fig. 5f). We also quantified the distribution of both emitter species along the z axis by taking into account the 3D curvature of the nuclear envelope, which was found through a spline interpolation of the pore positions (Methods). Thus, we recovered a distance of ~46 nm between the Nup96 layers with the WGA distribution centered in between (Fig. 5g), underscoring once more the 3D capability of MINFLUX nanoscopy.

Discussion

We have shown that MINFLUX nanoscopy can provide nanometer resolution in three dimensions, on arbitrary fields of views, in

living cells and using multiple color channels. While the current limitations of labeling have not allowed us to identify two switchable emitters at 1-3 nm distance, the resolution potential of MINFLUX nanoscopy is evidenced by the fact that it localized individual switchable fluorophores with a s.d. of below 1-3 nm in 3D. Yet, the full potential of this method has not been reached. Ongoing and future developments will cut down the current recording time from tens of minutes per 500 localizations. This can be achieved by optimizing the activation procedure, registering more than just one molecule per localization and minimizing the fluorophoreto-zero average distance. As the minimal fluorophore-to-zero average distance is determined by the background in the imaged region⁵, we will explore time-gated detection and multiphoton excitation for background reduction in the future. When imaging densely filled 3D structures, limitations may arise from collateral activation of fluorophores outside the MINFLUX imaging region resulting in a lower apparent labeling efficiency. Yet these limitations can be addressed by identifying or developing activatable fluorophores with more stable off-states. Note that the excitation powers used in this work are on the order of 20-60 µW, so that the intensities (10-50 kW cm⁻² at the peak of the donut beam) are comparable to those used in biological confocal microscopy, where the power is focused to an area about three times smaller than that of the donut beam.

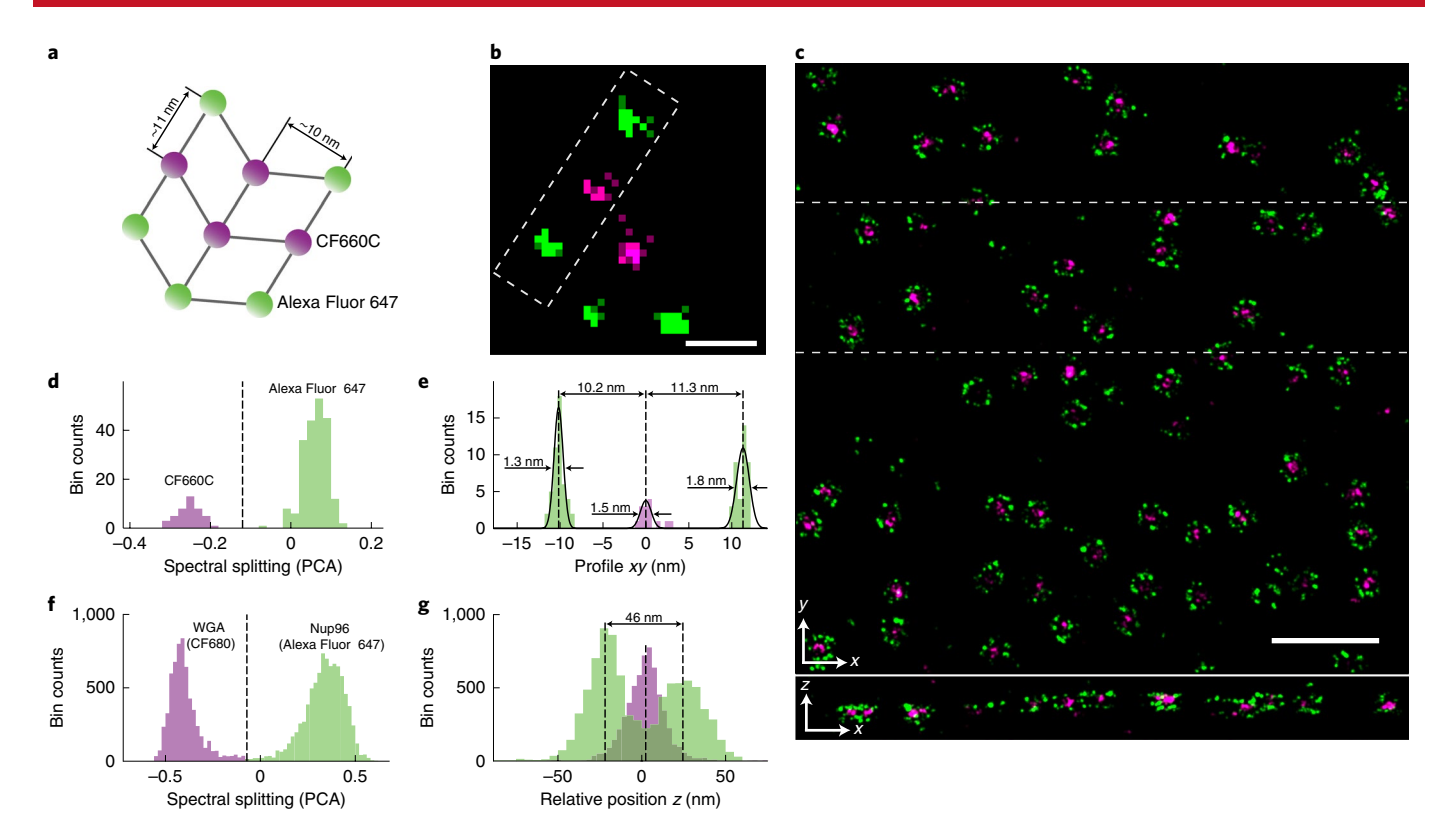


Fig. 5 | Two-color MINFLUX nanoscopy in 2D and 3D. a, Scheme of a DNA origami labeled with Alexa Fluor 647 and CF660C with ~10 nm intermolecular distances. **b**, Histogram of the localizations acquired with 2D MINFLUX. Alexa Fluor 647 is shown in green, CF660C in magenta. Dashed lines indicate the expected molecule positions. **c**, Two-color image of U-2 OS cell expressing Nup96-SNAP. The SNAP-tag was labeled with Alexa Fluor 647. Additionally, WGA conjugated to CF680 stained the center of the NPC. **d**, Spectral separation of the two fluorophore species. The abscissa is the principal component of the detection probability on the spectral channel with λ < 685 nm for all iterations. The spectral separation (dashed line) minimizes overlap between the two species. **e**, Histogram of localizations along the box in **b** together with Gaussian fit curves for each molecule position. The fit delivered the displayed FWHM values and intermolecular distances. **f**, Spectral distribution of the two fluorophore species with choice of color separation (dashed line). **g**, *z* distribution of the two fluorophore species. After considering the nuclear envelope shape (see Fig. 3f) for each nuclear pore position, a distance of 46 nm is found between the cytoplasmic and nucleoplasmic layers of Nup96; WGA is aggregated at the pore center. Scale bars, 10 nm (**b**) and 500 nm (**c**).

As MINFLUX utilizes a scanning read-out, the recording time of MINFLUX nanoscopy scales with the imaged area or volume. However, an advantage of scanning is that one can adapt the activation rate to the local fluorophore concentration to save time. Another avenue is to parallelize scanning using sets of donuts or standing waves. Furthermore, one can utilize different on–off switching processes, such as the transient binding of fluorescent molecules like in PAINT²¹ or DNA-PAINT²². Note that for a PAINT-like sample preparation, the speed and precision advantages provided by MINFLUX persist.

With lens-based fluorescence microscopy having finally reached true nanometer resolution, it is important to bear in mind that fluorescence microscopes map nothing but the fluorophores; once the microscopes have fulfilled this task, they have accomplished their mission. Hence, any conclusion going beyond that, especially at sub-10-nm length scales, has to take the size and distance of the fluorophore to the target molecule into account, making the labeling method ever more crucial. MINFLUX offers more flexibility in this regard because, by requiring fewer detected photons than standard camera-based localization, a larger range of fluorophores and labeling procedures should be viable. For this reason, as well as its unique 3D imaging performance, MINFLUX is bound to be a cornerstone, if not the vanguard, of nanometer-scale fluorescence microscopy in the years to come.

Online content

Any methods, additional references, Nature Research reporting summaries, source data, extended data, supplementary information, acknowledgements, peer review information; details of author contributions and competing interests; and statements of data and code availability are available at https://doi.org/10.1038/s41592-019-0688-0.

Received: 12 August 2019; Accepted: 15 November 2019; Published online: 13 January 2020

References

- Hell, S. W. & Wichmann, J. Breaking the diffraction resolution limit by stimulated emission: stimulated-emission-depletion fluorescence microscopy. Opt. Lett. 19, 780–782 (1994).
- Klar, T. A., Jakobs, S., Dyba, M., Egner, A. & Hell, S. W. Fluorescence microscopy with diffraction resolution barrier broken by stimulated emission. *Proc. Natl Acad. Sci. USA* 97, 8206–8210 (2000).
- Rust, M. J., Bates, M. & Zhuang, X. Sub-diffraction-limit imaging by stochastic optical reconstruction microscopy (STORM). *Nat. Methods* 3, 793–795 (2006).
- Betzig, E. et al. Imaging intracellular fluorescent proteins at nanometer resolution. Science 313, 1642–1645 (2006).
- Balzarotti, F. et al. Nanometer resolution imaging and tracking of fluorescent molecules with minimal photon fluxes. Science 355, 606–612 (2017).
- 6. Hell, S. W. Far-field optical nanoscopy. Science 316, 1153-1158 (2007).

- Eilers, Y., Ta, H., Gwosch, K. C., Balzarotti, F. & Hell, S. W. MINFLUX monitors rapid molecular jumps with superior spatiotemporal resolution. *Proc. Natl Acad. Sci. USA* 115, 6117–6122 (2018).
- 8. Backlund, M. P., Shechtman, Y. & Walsworth, R. L. Fundamental precision bounds for three-dimensional optical localization microscopy with Poisson statistics. *Phys. Rev. Lett.* **121**, 023904 (2018).
- Thevathasan, J. V. et al. Nuclear pores as versatile reference standards for quantitative superresolution microscopy. Nat. Methods 16, 1045–1053 (2019).
- von Appen, A. et al. In situ structural analysis of the human nuclear pore complex. Nature 526, 140–143 (2015).
- Banterle, N., Bui, K. H., Lemke, E. A. & Beck, M. Fourier ring correlation as a resolution criterion for super-resolution microscopy. *J. Struct. Biol.* 183, 363–367 (2013).
- Nieuwenhuizen, R. P. J. et al. Measuring image resolution in optical nanoscopy. Nat. Methods 10, 557–562 (2013).
- Hell, S., Reiner, G., Cremer, C. & Stelzer, E. H. K. Aberrations in confocal fluorescence microscopy induced by mismatches in refractive index. *J. Microsc.* 169, 391–405 (1993).
- Masch, J.-M. et al. Robust nanoscopy of a synaptic protein in living mice by organic-fluorophore labeling. *Proc. Natl Acad. Sci. USA* 115, E8047–E8056 (2018).
- MacGillavry, H. D., Song, Y., Raghavachari, S. & Blanpied, T. A. Nanoscale scaffolding domains within the postsynaptic density concentrate synaptic AMPA receptors. *Neuron* 78, 615–622 (2013).

- 16. Fukata, Y. et al. Local palmitoylation cycles define activity-regulated postsynaptic subdomains. *J. Cell Biol.* **202**, 145–161 (2013).
- MacGillavry, H. D. & Hoogenraad, C. C. The internal architecture of dendritic spines revealed by super-resolution imaging: what did we learn so far? Exp. Cell Res. 335, 180–186 (2015).
- Zhang, Z., Kenny, S. J., Hauser, M., Li, W. & Xu, K. Ultrahigh-throughput single-molecule spectroscopy and spectrally resolved super-resolution microscopy. *Nat. Methods* 12, 935–938 (2015).
- Dai, M., Jungmann, R. & Yin, P. Optical imaging of individual biomolecules in densely packed clusters. *Nat. Nanotechnol.* 11, 798–807 (2016).
- Li, B. & Kohler, J. J. Glycosylation of the nuclear pore. *Traffic* 15, 347–361 (2014).
- Sharonov, A. & Hochstrasser, R. M. Wide-field subdiffraction imaging by accumulated binding of diffusing probes. *Proc. Natl Acad. Sci. USA* 103, 18911–18916 (2006).
- Jungmann, R. et al. Single-molecule kinetics and super-resolution microscopy by fluorescence imaging of transient binding on DNA origami. *Nano Lett.* 10, 4756–4761 (2010).

Publisher's note Springer Nature remains neutral with regard to jurisdictional claims in published maps and institutional affiliations.

© The Author(s), under exclusive licence to Springer Nature America, Inc. 2020

Methods

Experimental setup. Optical setup. We used an optical setup (Supplementary Fig. 1) that was based on a previously described microscope^{5,7}, with three different illumination modalities provided through separate optical paths: (i) widefield excitation (488 nm, 560 nm and 640 nm), (ii) regularly focused excitation (560 nm or 642 nm) or focused activation (405 nm) and (iii) phase-modulated excitation (560 nm or 642 nm) leading to a 2D or 3D donut in the focal region. For all excitation beams, we employed an acousto-optic tunable filter for slow power modulation and wavelength selection. Switching between the regularly focused and 2D and 3D donut excitation was performed with electro-optical modulators (EOM). To laterally position the MINFLUX beam within the TCP and to approach the molecules iteratively, we employed electro-optical deflectors, which were differentially driven with two pairs of identical amplifiers. To image larger fields of views, we scanned the focused activation beam and the TCP across the sample using a piezo-based tip-tilt mirror. An electro-optically actuated varifocal lens (VFL) positioned the 3D donut beam axially. The current implementation allowed scanning of the beam in a range of about $10 \times 10 \, \mu m^2$ in the lateral direction and 400 nm in the axial direction. The sample was translated using a manual as well as a piezo-driven sample stage. 2D and 3D donut generation was accomplished with a spatial light modulator. Applying an achromatic $\lambda/4$ retarder plate for circular beam polarization helped minimize the intensity at the donut minimum. To further ensure a deep minimum, we measured the aberrated wavefront using a pupil-segmentation-based scheme²³. A 1.4 numerical aperture oil immersion lens focused the excitation light into the sample and collected the fluorescence light. The tip-tilt mirror descanned the emitted light, which subsequently passed through a quad-band dichroic mirror. Electrically driven flip-mirrors allowed the selection between the following options: (i) a detection path for acquiring a fluorescence overview image of the sample with an electron-multiplying charge-coupled device (EMCCD) camera and selecting a region of interest; (ii) a large-area detector for measuring the point spread function (PSF) of the excitation beam; (iii) a confocal pinhole (multi-mode-fiber) of 500 nm (sample units) for MINFLUX fluorescence acquisitions.

An active stabilization system ensured nanometer stability of the sample (Supplementary Fig. 3). For lateral stabilization, we imaged nanometer-sized scattering gold nanorods (25 nm × 75 nm) onto a camera using a spectrally filtered white-light laser source (~950-1,000 nm). An infrared laser beam (905 nm) illuminated the sample in total internal reflection mode so that the axial position was accessible using another camera. A proportional-integral-derivative controller commanded the piezo-stage to compensate the movements. As MINFLUX relies on the precise knowledge of the shape and position of the excitation beam, we mapped the applied scanner voltage to a physical position in the sample by calibrating the xy scanners for both excitation lines⁵. Additionally, we calibrated the axial beam displacements (induced by the VFL) by measuring the axial position of the excitation PSF for different input voltages. We also took the refractive index mismatch between the coverglass and the sample into account. To this end, we performed a 3D MINFLUX measurement to determine the position of two Alexa Fluor 647 molecules on a DNA nanoruler (GATTA-STED 3D 90R custom, GATTAquant). We scaled the estimated z position to match the expected intermolecule distance. We confirmed the scaling factor of 0.70 in simulations²⁴ and applied it in post-processing to correct all estimated *z* localizations. Fluorescent microspheres (see below) were used to re-examine the alignment of the microscope on a daily basis. To this end, we verified the co-alignment of the activation beam, the regularly focused and the donut-shaped excitation beam. Moreover, we adjusted the confocal detection to coincide with the excitation volume. We measured the PSF of the excitation beams by scanning an area or volume around the donut minimum with the electro-optical deflectors or the tip-tilt mirror (xy) and the sample stage (z), respectively.

Experiment control software. Similarly to our previously published works^{5,7}, we used custom programs written in LabView (National Instruments) for control of the experimental setup and data acquisition. We implemented the control of hardware components using data acquisition boards (NI PCIe-6353), an FPGA board (NI USB-7856R) and through direct communication with devices (for example USB or serial port). The software package consisted of four types of programs: iterative MINFLUX FPGA core (see below; Supplementary Fig. 2 and Supplementary Table 1), iterative MINFLUX PC host, system stabilization and auxiliary device control. The iterative MINFLUX FPGA core served the following purposes: control of beam deflectors and amplitude modulators; selection of beam shape and type (activation or excitation); photon registration via avalanche photo diodes (APDs); online data processing; and position scanning for image acquisition. This program performed all tasks and processes described below. The MINFLUX FPGA core and PC host communicated via USB, delivering control commands from the host PC to the FPGA and streaming the acquired data and state information from the FPGA to the host PC.

Live position estimators. Position estimation for donut exposures. For 1D, 2D and 3D position estimation with a donut-shaped excitation beam, we used a modified version of the previously developed modified least mean square estimator (mLMSE)⁵. For position estimation in three dimensions, we performed a natural

extension of the estimator resulting in the same expression as equation S51 in ref. but with the beam positions $\bar{r}_{\rm b}$ now being three-dimensional vectors

$$\widehat{\widehat{r}}_{\mathrm{mLMS}}^{(k)} \Big(\widehat{\widehat{p}}, \overline{\beta} \Big) = -\frac{1}{1 - \frac{L^2 \ln(2)}{\mathrm{FWHM}^2}} \Big(\sum_{j=0}^k \beta_j \widehat{p}_0^j \Big) \sum_{i=0}^{m-1} \widehat{p}_i \cdot \overline{r}_{\mathsf{b}_i}$$

where m is the number of exposures (targeted coordinate positions), k is the estimator order, $\{\beta_j\}$ are the estimator parameters, L is the beam separation, FWHM is the full width at half maximum of a regularly focused beam (FWHM = 360 nm in this work) and $\{\hat{p}_i = n_i/N\}$ are the measured relative photon counts for the different exposures. We used an estimator order of k=1. The estimator parameters β_j were optimized numerically using a typical measured shape of the 2D donut or an ideal quadratic function approximating the minimum of the 3D donut and assuming a typical experimental signal-to-background ratio. For optimization of $\{\beta_j\}$ we used the Matlab function fmincon to minimize the mean bias of the mLMSE position estimate in a circular region (for 2D) or spherical volume (for 3D) with a diameter of 0.8L, with the beam separation L. We used the obtained position estimator parameters for the live position estimation in the MINFLUX FPGA core as well as for optimization of the iterative MINFLUX strategy.

Position estimation for regularly focused exposures. Position estimation using a regularly shaped excitation beam was performed using an estimator derived from the previously published estimator for position estimation in 1D using a TCP with a regularly focused beam and two exposures (see equation S40 in ref. 5). We modified the molecule position estimator \hat{x}_{m} to take into account background signal. The estimator used in this work takes the form

$$\hat{x}_{\rm m}^{\rm G}(n_0,N) = \left(1 + \frac{1}{{\rm SBR}}\right) \frac{{\rm FWHM}^2}{8\ln(2)L} [\ln(n_0) - \ln(N-n_0)],$$

where n_0 is the number of photons in the first exposure, N is the total number of detected photons, L is the beam separation of the two probing positions, FWHM is the full width at half maximum of the excitation beam (FWHM = 300 nm in this study) and SBR is the signal-to-background ratio. We used this estimator for live position estimation in the MINFLUX FPGA core as well as for optimization of the iterative MINFLUX strategy. The SBR was kept fixed for each measurement assuming a typical value for the sample of the study.

Simulations and optimization of iterative strategy. Different iterative MINFLUX schemes were investigated and optimized through numerical simulations using Matlab (MathWorks). We simulated the complete iterative localization scheme for a set of molecules within the volume covered by the activation beam $(360\times360\times360\times360\,\mathrm{nm})$, with the goal of finding the optimal number of iterations K, size of the TCP L_k and number of photons to use N_k . The simulation replicated the live estimations performed by the FPGA hardware, while the final localization was performed via the maximum likelihood estimator (MLE), which was used in post-processing. By minimizing the average localization error for all simulated molecule positions, the optimal iterative parameters $\{K, L_k, N_k\}$ were found. The beam shapes used in the simulation are shown in the table below.

Туре	Function	Variables
Gaussian detection	$f(\bar{x}) = \frac{e^{\left(-\frac{(x-x_0)^2}{2\sigma_{\text{DelXY}}^2}\right) \cdot e^{\left(-\frac{(y-y_0)^2}{2\sigma_{\text{DelXY}}^2}\right) \cdot e^{\left(-\frac{(z-z_0)^2}{2\sigma_{\text{DelX}}^2}\right)}}}{(2\pi)^{3/2} \cdot \sigma_{\text{DelXY}}^2 \cdot \sigma_{\text{DelX}}}$	$\sigma_{DetXY} : \frac{500nm}{2\sqrt{2ln(2)}}$ $\sigma_{DetZ} : \frac{1,000nm}{2\sqrt{2ln(2)}}$
Focused excitation	$f(\bar{x}) = \frac{e^{\left(\frac{(x-x_b)^2}{2\sigma_{GaussXY}^2}\right)} \cdot e^{\left(\frac{(y-y_b)^2}{2\sigma_{GaussXY}^2}\right)} \cdot e^{\left(\frac{(z-z_b)^2}{2\sigma_{GaussXY}^2}\right)}}{(2\pi)^{3/2} \cdot \sigma_{GaussXY}^2 \cdot \sigma_{GaussZ}}$	$\sigma_{GaussXY} : \frac{330 nm}{2\sqrt{2 ln(2)}}$ $\sigma_{GaussZ} : \frac{800 nm}{2\sqrt{2 ln(2)}}$
2D donut	$f(\bar{x}) = f_{PSF2d}(x - x_b, y - y_b) \cdot \frac{e^{\left(-\frac{(x - x_b)^2}{2\sigma_z^2}\right)}}{\sqrt{2\pi \cdot \sigma_Z}}$	$\sigma_Z: \frac{1,000 \text{nm}}{2\sqrt{2 \text{ln}(2)}}$ $f_{\text{PSF2d}}: \text{ experimental}$ 2D PSF
3D donut	$f(\bar{x}) = (x - x_b)^2 + (y - y_b)^2 + (z - z_b)^2$	

Data acquisition. Before starting a MINFLUX measurement, we selected a region of interest and moved the sample to the imaging plane on the basis of a widefield fluorescence acquisition. We defined scanning points in the selected region, located either on a rectangular grid or in a manually defined arrangement. Using a focused excitation beam with high intensity $(100-200\,\mu\text{W}$ entering the back focal plane of the objective lens), we transferred the fluorescent molecule population into a long-lived non-fluorescent state. We conditionally applied light of 405 nm wavelength $(0.5-5\,\mu\text{W})$ to photoactivate single molecules. Subsequently, we probed the presence of an emitting fluorophore by illuminating with excitation light using the configuration defined for the first iteration (typically 0.1 ms minimal time until collection of 40–100 photons) and comparing the low-pass-filtered photon count rate (filter constant 1–10 ms) to a predefined threshold (5–50 kHz). Upon detection

of a fluorescent molecule, we did not return to the activation step and continued the iterative MINFLUX acquisition scheme. During the iterations, we applied excitation powers in the range of $20-60\,\mu\text{M}$ in the back focal plane (comparable to confocal microscopy). The MINFLUX scheme ended either (i) upon the photon count rate falling below a threshold predefined for each iteration, meaning the molecule turned off or (ii) upon reaching a certain photon number in the last iteration. In case (i), activation light was applied. In case (ii), we restarted the MINFLUX iterations. After a predefined time with no single molecule events $(0.3-20\,\text{s})$ or a certain amount of activation pulses (10,000-30,000 pulses corresponding to $5-15\,\text{s}$ of 405-nm light illumination), the tip-tilt mirror moved the illumination beams to the next scan position. We selected the scan positions in a rectangular pattern with distances of $200-250\,\text{nm}$, ensuring a homogenous activation of the whole scan area. As a result, regions covered in neighboring scan positions were overlapping, so that a molecule between the scan positions could be approached starting from any of the neighboring positions.

A flow chart and pseudocode describing the data acquisition are provided in Supplementary Fig. 2 and Supplementary Table 1.

Data analysis. *PSF evaluation.* We measured the shape of the excitation point spread function (PSF) with samples of immobilized fluorescent microspheres (FluoSpheres, 0.02-µm, dark-red fluorescence; Thermo Fisher Scientific). For measurements in two dimensions, data acquisition and processing of the PSF followed a previously published protocol⁵. For measurement in three dimensions, we assumed the PSF to take the form $I(x,y,z) = a(x^2 + y^2 + z^2)$, with a denoting a constant.

Trace segmentation. In the photon count trace segments, we distinguished single molecule emissions from background using a hidden Markov model⁵. We only considered trace sections for which the MINFLUX acquisition was running in its final iteration. We obtained a first estimate for the emission rates in the hidden Markov model by calculating the mean emission after artificially splitting the median filtered photon counts at a manually chosen threshold in the range 1.1-3.6. We used a Poissonian distribution with the obtained mean emission values as initial emission probabilities in the hidden Markov model. Using the Matlab implementation of the Viterbi algorithm (Matlab function hmmviterbi), we estimated the emission states from a three-state hidden Markov model (1, on; 2, off; and 3, blinking) with the sampling time $t_s = 0.1$ ms, $t_{off} = 0.1$ s and $t_{on} = 0.5$ s being the estimated on and off times of the molecule and $t_{\text{blink,on}} = 1 \text{ ms}$ and $t_{\rm blink,off}$ = 0.1 ms the estimated blinking on and off times. We applied the Viterbi algorithm twice, using the same transition probability matrix, but applying the improved emission rate distribution from the previous run. We merged successive emissions in states 1 or 3. We split events at a predefined photon number of N=2,000 to obtain several localizations per molecule for an experimental assessment of the localization precision. We assigned a molecule identification number to each localization assuming that emissions with several iteration rounds (no activation applied in between) originated from the same molecule.

Position estimation. We used a maximum likelihood estimator implemented in a grid-search optimization algorithm to retrieve the molecule positions from the photon count traces⁵. For the 3D MINFLUX scheme, we wrote the trivial extension of the *p* functions to three dimensions using the presented TCP. Unlike before, we could not obtain the background counts directly from the measurement as the background depended on (i) the position in the scan and (ii) the position of the iterative TCP in the confocal volume, so that the background varied even for successive events of the same molecule. We circumvented this issue by estimating the signal-to-background ratio (SBR) with the molecule position in the maximum likelihood estimator.

To obtain an estimate of the true SBR distribution for a given measurement, we determined the SBR of individual events by comparing the emission rate after the off-switching to the emission rate during the event on the basis of the previously estimated emission states. The resulting SBR distributions are shown in Supplementary Fig. 5.

Event filtering. During the iterative MINFLUX measurement, we chose a fixed threshold value to decide on the presence of a molecule emission. This approach led to two types of false positives: (i) reaction to background, as we chose a low threshold value to avoid missing faint emission events; and (ii) reaction to thermally activated molecules outside the iterative MINFLUX region, which were still detected, despite the live estimators not reaching them.

We applied three filters in post-processing to select true emission events only. These are the central donut fraction p_0 , the estimated location of the molecule with respect to the center of the TCP $r_{\rm rel}$ and the photon number in the last iteration N. We show the distribution of the filtering variables together with the selected threshold values in Supplementary Figs. 4, 8 and 9 for all presented datasets.

Molecules far outside the TCP and background events are expected to produce equal mean counts in all m exposures, delivering $p_0^{(b)} \sim 1/m$, with $p_0 = n_0 / \sum_{i=0}^{m-1} n_i$ describing the probability to detect a photon in the central exposure. True emission events will yield $p_0 < 1/m$ when successfully approaching the molecule in the iterations. The overlap of the two distributions becomes stronger with decreasing SBR, so that a classification on the basis of p_0 was not

sufficient in a cellular context. We achieved a better classification by using the distance of the estimated position with respect to the center of the TCP in the last iteration $r_{\rm rel} = \left(x_{\rm rel}^2 + y_{\rm rel}^2 + z_{\rm rel}^2\right)^{1/2}$, a measure that does not directly depend on the SBR. We note that further restricting both filter variables can improve the overall localization precision at the expense of discarding valid localizations. For measurements with a population of events with low photon number, we additionally applied a lower threshold on the photon number N in the last iteration to avoid a bias in the position estimation.

In the case of the two-color DNA origami, we observed outliers in the average count rate during an emission event, which most likely appeared owing to an interaction of nearby fluorophores. For this reason, we omitted localizations with an average count rate larger than 50 kHz.

We should note that, by recording molecular traces, we can detect the simultaneous occurrence of more than one fluorophore much better than camera-based localization schemes. The appearance or disappearance of a second molecule is visible as a step in the emission trace or absolute count rate. In the unlikely case that a second molecule appears within the MINFLUX region, the count rate is roughly doubled. If not filtered out, this will result in a localization in between the molecules with the position scaled by the relative effective brightness of the involved emitters. If a second fluorophore appears outside the MINFLUX region owing to thermal activation or activation by the excitation beam, the event is discarded by the filters decribed above. To reduce the probability of simultaneous activation as much as possible, we applied the activation light conditionally, meaning that we switched the light off as soon as a single molecule appeared.

 $Multicolor\ classification.$ For each localization, we obtained photon numbers for both spectral channels in all iterations. We used the probability of detecting a photon in the blue-shifted spectral channel in the ith iteration

$$p_{\mathrm{blue}}^{(i)} = \frac{N_{\mathrm{blue}}^{(i)}}{N_{\mathrm{blue}}^{(i)} + N_{\mathrm{red}}^{(i)}}$$

as a measure of the spectral properties of the dye. In the last iteration, we obtained mean values of 0.2, 0.4 and 0.55 for CF680, CF660C and Alexa Fluor 647, respectively. Photons from all MINFLUX iterations carry information about the spectral properties of the dye, but with different signal-to-background ratio values. To reduce the classification error by using all available information, we performed a principal component analysis on the basis of $p_{\rm blue}^{(i=0,\dots\,{\rm max(iter)})}$ and manually chose a splitting threshold to classify the dye species on the basis of the distribution of the first principal component.

Image rendering. In datasets with a low number of events per molecule, we replaced each localization with a Gaussian distribution, summing up pixel entries for overlapping Gaussians. We normalized the image, resulting in $0 \le I_{ij} \le 1$ with I_{ij} being the value of the ijth pixel. For images displaying a micrometer-sized image region (Figs. 2a and 5e), we chose a pixel size of 0.5 nm and a large-width Gaussian kernel (σ = 4 nm) for visibility. For images displaying single or few nuclear pores (Fig. 2a,f) we chose σ = 2 nm and a pixel size of 0.2 nm. We used a non-linear color distribution to compensate for the unequal number of events per fluorescent molecule. For the multicolor data (Fig. 5e), we independently convolved the localization of each dye species with a Gaussian kernel and displayed the normalized images as RGB images with α =7 in the red channel and α =5 in the green channel using the components

$$I_{ij}^{(\mathrm{red})} = \alpha \cdot I_{ij}^{(\mathrm{CF660C, CF680})}$$

$$I_{ii}^{(\text{green})} = \alpha \cdot I_{ii}^{(\text{Alexa Fluor 647})}$$

$$I_{ij}^{(\text{blue})} = 0.7 \cdot I_{ij}^{(\text{CF660C,CF680})}$$

For the DNA origami image (Fig. 5b), we displayed a simple 2D histogram of the localization data with 1-nm pixel size, with the RGB value for each pixel determined with $\alpha\!=\!0.5$. Where we displayed localization data as scatter plots, the size of the scatter points or spheres was unrelated to the estimated localization precision. An exception is Fig. 2e, where we displayed scatter points together with an ellipse, with the principal axes lengths relating to the localization precision.

Surface fitting. To obtain a model of the nuclear envelope in the 3D measurements of nuclear pore complexes (Figs. 3f and 5e), we first determined the nuclear pore centers by clustering localization in the same nuclear pore. We employed the Matlab implementation linkage to generate an agglomerative hierarchical cluster tree using the median as a distance measure between clusters. We chose clusters using the Matlab cluster function on the basis of the manually determined number of clusters in the data. On the basis of the mean position of all clusters in the dataset, we approximated the shape of the nuclear envelope using thin-plate smoothing spline interpolation with a smoothing parameter of 0.999 (Matlab function tpaps).

For surface fitting of PSD-95, localizations were assigned to two domains using a k-means-clustering algorithm. To determine the average position of the volumes of high localization density within each domain, we employed the Matlab implementation of the density-based clustering algorithm dbscan (epsilon = 8 nm, minPts=10). We determined a surface using the Matlab function tpaps with a smoothing parameter 0.996.

Performance metrics. We assessed the localization precision in the acquired MINFLUX images using clustering of localizations according to their molecule identification number. This included grouping localizations from single iteration cycles, obtained by splitting the photon numbers in time, as well as grouping localizations from subsequent iterations that were triggered by exceeding a predefined photon number in the last iteration. We filtered for molecules with more than four localizations. We calculated the s.d. of single clusters and obtained the median s.d. for all molecules (Figs. 2b and 3i). To achieve a more general assessment (Figs. 2c, 3h and 4c), we subtracted the mean cluster position from all localizations and displayed the obtained distances in 1D histograms for all three dimensions. We assumed a Gaussian distribution of the distances to determine their spread in a fit. We note that calculation of the mean cluster position was biased for a low number of samples, which lead to a slight bias toward lower values in the localization precision that we obtain.

We used an FRC analysis to assess the resolution in the image independently of any localization clustering. We randomly split the localizations in two groups and determined the FRC curve directly from the localization coordinates as previously described²⁵. We chose a correlation threshold of 1/7 to determine the spatial frequency transition from signal-to-background¹². To reduce noise in the determination of the cut-off frequency, we interpolated the data using the 'nearest' method of the Matlab function interp1.

Sample preparation. Sample mounting and imaging buffers. To stabilize the sample during the MINFLUX acquisition, we treated all coverslips with gold nanorods (A12-25-980-CTAB-DIH-1-25, Nanopartz). We diluted the nanorods 1:3 in single-molecule clean PBS (P4417, Sigma-Aldrich), sonicated them for 5–10 min and incubated the sample with the nanorod solution for 5–10 min at room temperature. To avoid floating nanorods, we washed the sample three to four times in PBS after removing the nanorod solution.

For MINFLUX imaging of samples labeled with Alexa Fluor 647, CF660C or CF680, we used a STORM blinking buffer containing $0.4\,\mathrm{mg\,ml^{-1}}$ glucose oxidase (Sigma-Aldrich, G2133), $64\,\mu\mathrm{g\,ml^{-1}}$ catalase (Sigma-Aldrich, C100-50MG), $50\,\mathrm{mM}$ Tris-HCl, pH 8.0 or 8.5, $10\,\mathrm{mM}$ NaCl, $10{-}30\,\mathrm{mM}$ MEA (cysteamine hydrochloride; Sigma-Aldrich, M6500) and 10% (wt/vol) glucose.

When measuring DNA origami samples, we added $10\,\rm mM~MgCl_2$ to the blinking buffer to avoid dehybridization of DNA strands.

We imaged U-2 OS cells endogenously tagged with mMaple in $50\,\text{mM}$ Tris buffer (pH 8) in 95% D₂O to reduce the short time blinking and increase the photon count of mMaple²⁶. We sealed the samples with picodent twinsil speed 22 (picodent).

Fluorescent microsphere sample. We used samples with poly-L-lysin-immobilized fluorescent microspheres (FluoSpheres, 0.02-μm, dark-red fluorescence; Thermo Fisher Scientific) to examine the setup performance on a daily basis, to measure the PSF of the optical setup and to calibrate the axial beam positioning with the VFL. The samples were prepared as previously described⁵.

DNA origami. We preannealed the unlabeled DNA origami template using a tenfold excess of the staple strands (containing biotinylated strands for immobilization) relative to the scaffold strands (M13mp18, N4040S, New England Biolabs) in folding buffer containing TAE 1× (1:5) and 27 mM MgCl₂, heating the mixture to 85 °C for 3 min, cooling down at a speed of 0.5 °C min⁻¹ until reaching 42 °C and storing at 4 °C. The sequences of the DNA staple strands are listed in Supplementary Table 3. After annealing, we purified the DNA origami templates by adding 15% PEG in TAE 1× containing 0.5 mM NaCl and 16 mM MgCl $_{\!\scriptscriptstyle 2}$ After mixing the solutions, we centrifuged for 30 min, keeping the sample at 4 °C. After removing excess, we repeated the procedure three times before storing the template in TAE 1× containing 10 mM MgCl₂. Before experiments, we annealed the template with the complementary strands 5'-labeled with a fluorescent molecule. In a first step, we used a 25× excess of the labeled strands and kept the mixed solutions overnight at room temperature. After purifying as described above, we repeated annealing and purification with a 250× excess of labeled strands. On the day of the experiment, we prepared the samples with immobilized DNA origamis as previously described5.

U-2 OS Nup96 cells. We handled the cells as previously described[®]. In brief, cells were cultured in DMEM without phenol red (1180-02, Thermo Fisher Scientific) supplemented with 1× MEM NEAA (11140-035, Thermo Fisher Scientific), ZellShield (13-0050, Minerva Biolabs), 1× GlutaMAX (35050-038, Thermo Fisher Scientific) and 10% (vol/vol) FBS (10270-106, Thermo Fisher Scientific) at 37 °C, 5% CO₂ and 100% humidity. For live-cell measurements (Nup96−mMaple), seeded coverslips were mounted and imaged as described above.

For measurement of fixed cells (Nup96-mMaple and Nup96-SNAP), seeded coverslips were prefixed (2.4% (wt/vol) formaldehyde in PBS) after 2 d of growth for 30 s, permeabilized (0.4% (vol/vol) Triton X-100 in PBS) for 3 min and fixed (2.4% (wt/vol) formaldehyde in PBS) for 30 min. The sample was quenched by incubating it for 5 min in 100 mM NH₄Cl and subsequently washed twice for 5 min in PBS. Samples of Nup96-mMaple were ready for imaging and mounted as described above. Nup96-SNAP samples were blocked for 30 min with Image-iT FX Signal Enhancer (Thermo Fisher Scientific) and stained with staining solution $(1\,\mu\text{M}\ BG\text{-AF647}\ (S9136S,\ New\ England\ Biolabs),\ 1\,\text{mM}\ dithiothreitol\ in\ 0.5\%$ (wt/vol) BSA) for 50 min. After washing three times in PBS for 5 min each to remove unbound dye, the samples were mounted as described above. For cells with an additional labeling for the center of the pore, we applied the WGA–CF680 conjugate (29029, Biotium) diluted to $0.02\,\mu g\,ml^{-1}$ in PBS with the addition of 1% BSA in the final solution. We incubated the cells at room temperature for 5 min before washing three times in PBS. The cell lines are available via Cell Line Services (Nup96-SNAP, 300444; Nup96-mMaple, 300461). Details on the cell lines used can be found in the Life Science Reporting Summary published with this article.

Hippocampal cultured neurons (PSD-95). We prepared hippocampal neurons from transgenic PSD-95–HaloTag mice¹⁴ as previously described²⁷ in accordance with the Animal Welfare Law of the Federal Republic of Germany (Tierschutzgesetz der Bundesrepublik Deutschland, TierSchG) and the regulations about animals used in experiments (Tierschutzversuchsverordnung). After 35 d in vitro we fixed the neurons in paraformaldehyde (4% in PBS, pH 7.4) at room temperature for 15 min. After washing in PBS, we treated the neurons with NH₄Cl (100 mM) for 10 min to reduce background caused by autofluorescence. We permeabilized using 0.1% Triton X-100 in PBS for 10 min and subsequently stained with Alexa Fluor 647–HaloTag ligand (1 μ M, synthesized in house) for 30 min at room temperature. After several short washing steps in PBS, we mounted the coverslips for imaging as described above.

Statistics and reproducibility. The presented data show representative recordings of our experiments. We have repeated all experiments several times with different rounds of sample preparation. We obtained similar results for all experiments and they showed low statistical variation.

For each of the experiments with Nup96 labeling in U-2 OS cells (Figs. 2a,f, 3f and 5e, Supplementary Fig. 7a and Supplementary Videos 1 and 3) we imaged cells from at least ten different coverslips, which were taken from more than three different cell culture passage numbers and preparation.

Imaging of PSD-95 in hippocampal neurons (Fig. 4a and Supplementary Video 2) was performed for more than four synapses on two coverslips taken from the same neuron preparation.

We monitored the stability of the optical setup (Supplementary Fig. 3b–e) regularly and observed similar stability values. For all measurements shown, we visually checked the stage and sample stability values measured by the locking system (Supplementary Fig. 3b,d) during the experiment.

Reporting Summary. Further information on research design is available in the Nature Research Reporting Summary linked to this article.

Data availability

The data that support the findings of this study are available from the corresponding author S.W.H. upon reasonable request.

References

- Gao, P., Prunsche, B., Zhou, L., Nienhaus, K. & Nienhaus, G. U. Background suppression in fluorescence nanoscopy with stimulated emission double depletion. *Nat. Photonics* 11, 163–169 (2017).
- Leutenegger, M., Rao, R., Leitgeb, R. A. & Lasser, T. Fast focus field calculations. Opt. Express 14, 11277–11291 (2006).
- Pham, T.-A., Soubies, E., Sage, D. & Unser, M. Closed-form expression of the Fourier ring-correlation for single-molecule localization microscopy. https:// doi.org/10.1109/ISBI.2019.8759279. In *IEEE International Symposium on Biomedical Imaging* (IEEE, 2019).
- Ong, W. Q., Citron, Y. R., Schnitzbauer, J., Kamiyama, D. & Huang, B. Heavy water: a simple solution to increasing the brightness of fluorescent proteins in super-resolution imaging. *Chem. Commun.* 51, 13451–13453 (2015).
- D'Este, E., Kamin, D., Göttfert, F., El-Hady, A. & Hell, S. W. STED nanoscopy reveals the ubiquity of subcortial cytoskeleton periodicity in living neurons. *Cell Rep.* 10, 1246–1251 (2015).

Acknowledgements

We thank the following MPI colleagues: E. D'Este for support with biological sample optimization; M. Bates for discussions about single-molecule techniques; H. Ta for help with DNA origami; D. Kamin and I. Herfort for support with cultured neurons; the Facility for Synthetic Chemistry for the Alexa Fluor 647-HaloTag ligand. We acknowledge S. Grant (University of Edinburgh) for providing the PSD-95-Halo mouse

line. J. Thevathasan, B. Nijmeijer, M. Kueblbeck and U. Matti (all EMBL) made the Nup96 cell lines. P.H. and J.R. acknowledge the European Research Council (ERC grant CoG-724489) and the Human Frontier Science Program (grant RGY0065/2017 to J.R.). S.W.H. acknowledges support from DFG grant SFB1286/A7.

Author contributions

K.C.G., J.K.P. and F.B. designed and built hardware, programmed software and performed experiments and data analysis with input from S.W.H. K.C.G., J.K.P. and P.H. prepared samples. P.H. and J.R. proposed the Nup96 cell line as a resolution test sample. J.E. made the Nup96 cell line. F.B. carried out theoretical analysis of iterative MINFLUX with K.C.G. and co-supervised the project. S.W.H. supervised the project and was responsible for its conception. K.C.G., J.K.P., F.B. and S.W.H. wrote the manuscript.

Competing interests

S.W.H. is a co-founder of the company Abberior Instruments, which commercializes super-resolution microscopy systems, including MINFLUX. S.W.H., K.C.G. and F.B. hold patents on the principles, embodiments and procedures of MINFLUX.

Additional information

Supplementary information is available for this paper at https://doi.org/10.1038/s41592-019-0688-0.

Correspondence and requests for materials should be addressed to S.W.H.

Peer review information Rita Strack was the primary editor on this article and managed its editorial process and peer review in collaboration with the rest of the editorial team.

Reprints and permissions information is available at www.nature.com/reprints.

natureresearch

Corresponding author(s):	Stefan W. Hell
Last updated by author(s):	Nov 10, 2019

Reporting Summary

Nature Research wishes to improve the reproducibility of the work that we publish. This form provides structure for consistency and transparency in reporting. For further information on Nature Research policies, see <u>Authors & Referees</u> and the <u>Editorial Policy Checklist</u>.

Statistics				
1	es, confirm that the following items are present in the figure legend, table legend, main text, or Methods section.			
n/a Confirmed				
The exact sam	ple size (n) for each experimental group/condition, given as a discrete number and unit of measurement			
A statement o	n whether measurements were taken from distinct samples or whether the same sample was measured repeatedly			
	test(s) used AND whether they are one- or two-sided ests should be described solely by name; describe more complex techniques in the Methods section.			
A description	A description of all covariates tested			
A description	A description of any assumptions or corrections, such as tests of normality and adjustment for multiple comparisons			
A full descript AND variation	ion of the statistical parameters including central tendency (e.g. means) or other basic estimates (e.g. regression coefficient) (e.g. standard deviation) or associated estimates of uncertainty (e.g. confidence intervals)			
	hesis testing, the test statistic (e.g. F , t , r) with confidence intervals, effect sizes, degrees of freedom and P value noted exact values whenever suitable.			
For Bayesian a	analysis, information on the choice of priors and Markov chain Monte Carlo settings			
For hierarchic	al and complex designs, identification of the appropriate level for tests and full reporting of outcomes			
Estimates of e	ffect sizes (e.g. Cohen's d , Pearson's r), indicating how they were calculated			
1	Our web collection on <u>statistics for biologists</u> contains articles on many of the points above.			
Software and c	ode			
Policy information abou	ut availability of computer code			
Data collection	Custom written software in LabView 2016			
Data analysis	Custom written software in Matlab 2018b			
	om algorithms or software that are central to the research but not yet described in published literature, software must be made available to editors/reviewers. deposition in a community repository (e.g. GitHub). See the Nature Research guidelines for submitting code & software for further information.			
Data				
Accession codes, uniA list of figures that	ut <u>availability of data</u> nclude a <u>data availability statement</u> . This statement should provide the following information, where applicable: ique identifiers, or web links for publicly available datasets have associated raw data restrictions on data availability			
The data that support the	e findings of this study are available from the corresponding author S.W.H. upon reasonable request.			
Field-speci	fic reporting			
Please select the one b	elow that is the best fit for your research. If you are not sure, read the appropriate sections before making your selection.			
∠ Life sciences	Behavioural & social sciences Ecological, evolutionary & environmental sciences			

For a reference copy of the document with all sections, see <u>nature.com/documents/nr-reporting-summary-flat.pdf</u>

Life sciences study design

All studies must dis	sclose on these points even when the disclosure is negative.			
Sample size	No sample size calculation was done. For each sample more than 4 cells from at least two coverslips were imaged. For Nup96 experiments, the coverslips were taken from different cell culture passage numbers and preparations for covering biological variations of the samples. The measurements resulted in low statistical variation.			
Data exclusions	Only data that were obviously failing (like wrong microscope configuration or wrong manual focusing) were excluded. The exclusion criteria were pre-established.			
Replication	All replications were successful.			
Randomization	Samples were not randomized. Our experimental workflow did not allow/need randomization			
Blinding	No blinding was done. Our experimental workflow did not allow/need blinding			
Reportin	g for specific materials, systems and methods			
	ion from authors about some types of materials, experimental systems and methods used in many studies. Here, indicate whether each material, ted is relevant to your study. If you are not sure if a list item applies to your research, read the appropriate section before selecting a response.			
Materials & ex	perimental systems Methods			

Involved in the study

Flow cytometry

MRI-based neuroimaging

ChIP-seq

n/a

Clinical data
Eukaryotic cell lines

Involved in the study

Eukaryotic cell lines

Animals and other organisms Human research participants

Palaeontology

Antibodies

n/a

Policy	information	about	cell lines	
--------	-------------	-------	------------	--

Cell line source(s) ATCC-HTB-96, Lot # 61074667. The cells can be obtained via Cell Line Services (CLS, clsgmbh.de, Nup96-SNAP #300444, Nup96-mMaple #300461). Authentication Cell lines were not further authenticated. Mycoplasma contamination Cell lines have been tested and are negative for mycoplasma contamination. Commonly misidentified lines No commonly misidentified cell lines were used. (See ICLAC register)

Animals and other organisms

Policy information about studies involving animals; ARRIVE guidelines recommended for reporting animal research

PSD-95-HaloTag knock-in mice (C57BI/6J background) were kindly provided by Seth G.N. Grent (Edinburgh University, United Laboratory animals Kingdom) and bred in-house for several generations. No wild animals were involved. Wild animals Field-collected samples No samples collected from the field were used. Ethics oversight Cultures of hippocampal neurons were prepared in accordance with the Animal Welfare Law of the Federal Republic of Germany (Tierschutzgesetz der Bundesrepublik Deutschland, TierSchG) and the regulation about animals used in experiments (Tierschutzversuchsverordnung). Sacrificing of animals is not an experiment on animals according to TierSchG, so that no specific authorizationor notification is required.

Note that full information on the approval of the study protocol must also be provided in the manuscript.